

Heating of the IGM by FR II radio sources

Christian R. Kaiser^{1,2*} and Paul Alexander¹

¹ *MRAO, Cavendish Laboratory, Madingley Road, Cambridge, CB3 0HE, UK*

² *University of Oxford, Department of Physics, Nuclear Physics Laboratory, Keble Road, Oxford, OX1 3RH, UK*

6 September 2018

ABSTRACT

We present results of a numerical integration of the hydrodynamical equations governing the self-similar, two-dimensional gas flow behind the bow shock of an FR II radio source embedded in an IGM with a power law density profile. The model predicts pressure gradients within the cocoons consistent with modest backflow. For very steep external density profiles sources may well not expand in a self-similar fashion and in this case the model is not self-consistent. The assumption of ram pressure confinement of the cocoons perpendicular to the jet axis is found to overestimate the ratio of the pressure in front of the radio hot spots and that in the cocoons. Based on the properties of the gas between bow shock and cocoon we calculate the X-ray surface brightness of the flow. This emission is found to be a good tracer of the density distribution within the flow and varies significantly with the properties of the unshocked IGM. The cooling-time of the shocked IGM is found to be comparable to, or greater than, the Hubble time. The influence of a radio source on the evolution of its gaseous surroundings therefore extends well beyond the limited life time of the source itself. We compare our results with the X-ray map of Cygnus A and find some evidence for cold, dense gas clumps in the surroundings of this object. The extended X-ray emission observed around 3C 356 may also be caused by the bow shock of this radio source. We also present an empirical model for the X-ray emission of the shocked IGM due to thermal bremsstrahlung.

Key words: hydrodynamics – galaxies: active – galaxies: individual: Cygnus A – galaxies: individual: 3C 356 – galaxies: jets – X-rays: galaxies

1 INTRODUCTION

Most analytical models of FR II extragalactic radio sources are based on the existence of two jets emerging from an AGN in the core of the source; a model first proposed by Rees (1971). After passing through a strong shock at the location of the radio hot spot, the jet material inflates a cavity of hot, rarefied gas. The expansion of this cocoon is supersonic with respect to the surrounding IGM and therefore drives a bow shock into this material. This shock will compress and heat the gas of the IGM, thereby increasing X-ray emission from thermal bremsstrahlung. Inferred on theoretical grounds by Scheuer (1974), this hot layer of gas between bow shock and cocoon was first observed in Perseus A by Böhringer *et al.* (1993) and in Cygnus A by Carilli *et al.* (1994). The extended X-ray emission detected in the vicinity of 3C 356 (Crawford & Fabian 1996) may represent another example of

thermal bremsstrahlung of the IGM boosted by the presence of a powerful radio source.

The first analytical investigation of a cavity expanding supersonically into a surrounding atmosphere was presented by Sedov (1959) who considered the case of a strong explosion in a uniform density profile. Dyson *et al.* (1980) extended this analysis to spherically symmetric winds with a permanent energy input and Heinz *et al.* (1998) included density gradients by modeling the external density distribution with a King (1972) profile. The solutions of Sedov and Dyson *et al.* are both self-similar. The expansion of both the cocoons and bow shocks of FR II sources is shown to be self-similar regardless of its geometrical shape by Kaiser & Alexander (1997) (hereafter KA), and this result suggests that a solution based on the spherically symmetric case may be possible for a radio source provided that the elongation of the cocoon along the axis of the jet can be accommodated. The solution for the flow of the shocked IGM between bow shock and cocoon requires solution of at least a two-dimensional problem instead of the one-dimensional spherical case of an explosion or wind.

In this paper we assume the bow shock surrounding

* present address:
Max-Planck-Institut für Astrophysik, Karl-Schwarzschild-Str. 1,
85740 Garching, Germany. email: ckaiser@mpa-garching.mpg.de

the cocoon of FR II radio sources to be elliptical. We then determine the properties of the shocked gas between bow shock and cocoon by integrating numerically the relevant hydrodynamical equations. Analogous to KA, we will assume that the density distribution of the IGM surrounding the radio source is well described by a power law of the form $\rho_o(r/a_o)^{-\beta}$, where r is the radial distance from the centre of the distribution.

Although we may choose the shape of the bow shock freely without violating the conditions for self-similar expansion of the cocoon or bow shock, we will show that another condition for self-similarity may not be fulfilled by some of the solutions presented here. This condition is the pressure equilibrium of the jets within the uniform pressure of the cocoon away from the hot spots. This implies that for these cases the model may not be self-consistent. One possibility, as we discuss, is that the assumption of an elliptical shape for the bow shock must be relaxed and the source expands self-similarly with a somewhat modified shape. However, we believe that the results obtained in this paper are an important first step in solving the problems posed by the flow between bow shock and cocoon of FR II sources.

The general dynamics of the large-scale structure of FR II sources depends on the details of the confinement of the cocoons of these objects. It is usually assumed that the pressure of the material in the cocoon is balanced by the ram pressure of the IGM (e.g. Scheuer 1974, KA). In this paper we show that the assumption of ram pressure confinement of the cocoons overestimates the ratio of the pressure in front of the hot spot and that of the cocoon material, leading to lower hot spot advance speeds in the analysis of KA.

The results of the integration of the hydrodynamical equations allows us to determine the X-ray surface brightness of the shocked material. The result of this calculation can be directly compared with X-ray observations. The only currently available X-ray map of a powerful FR II source with sufficient spatial resolution to allow such a comparison, is the *ROSAT* map of Cygnus A presented by Carilli *et al.* (1994). However, the advent of the new X-ray telescopes such as *AXAF* will allow us to extend this analysis to a greater number of FR II sources.

In Section 2 we transform the hydrodynamical equations to an elliptical coordinate system comoving with the self-similar expansion of the bow shock and the cocoon. Section 3 describes the numerical method used to integrate the equations. The properties of the flow are discussed in Section 4. In Section 5 we calculate the X-ray emission as predicted by the model and compare our results with the X-ray maps of Cygnus A and 3C 356.

2 THE HYDRODYNAMICAL EQUATIONS IN AN ELLIPTICAL COORDINATE SYSTEM

The hydrodynamical equations governing adiabatic fluid flow in three dimensions if gravitational fields and viscosity can be neglected, are the equation of motion:

$$\frac{\partial}{\partial t} \mathbf{v} + (\mathbf{v} \cdot \nabla) \mathbf{v} = -\frac{1}{\rho} \nabla p, \quad (1)$$

the equation of continuity:

$$\frac{\partial}{\partial t} \rho + \nabla \cdot (\rho \mathbf{v}) = 0 \quad (2)$$

and the adiabatic equation:

$$\frac{\partial}{\partial t} \frac{p}{\rho^\Gamma} + (\mathbf{v} \cdot \nabla) \frac{p}{\rho^\Gamma} = 0, \quad (3)$$

where \mathbf{v} is the velocity vector of the gas, p the pressure, ρ its density and Γ its adiabatic index. We assume in the following analysis that the bow shock surrounding the cocoon is a prolate ellipsoid with rotational symmetry about the z -axis defined by the jet, and therefore we rewrite these equations in prolate spheroidal coordinates $(\eta, \xi, \phi = \pi/2)$, see Appendix A.1.1). The rotational symmetry reduces the problem to two spatial dimensions.

$$\begin{aligned} c c_r \frac{\partial}{\partial t} \mathbf{v}' + (\mathbf{v}' \cdot \nabla') \mathbf{v}' &= -\frac{1}{\rho'} \nabla' p', \\ c c_r \frac{\partial}{\partial t} \rho' + \nabla' \cdot (\rho' \mathbf{v}') &= 0, \\ c c_r \frac{\partial}{\partial t} \frac{p'}{\rho'^\Gamma} + (\mathbf{v}' \cdot \nabla') \frac{p'}{\rho'^\Gamma} &= 0, \end{aligned} \quad (4)$$

where all dashed quantities are functions of the elliptical coordinates η and ξ , c is constant and $c_r = (\sinh^2 \eta + \sin^2 \xi)^{1/2}$.

As the bow shock expands it is possible for all times to find a stationary prolate spheroidal coordinate system characterized by a constant c in which the bow shock is described as a coordinate surface with constant $\eta = \eta_b$. The aspect ratio of the cocoon, i.e. the ratio of its length to its width, R_b , and the ‘length’ of the bow shock, i.e. the point at which the cut of the bow shock with the xz -plane crosses the z -axis, determine the particular set of values for c and η_b . KA show that the expansion of the bow shock and of the cocoon is self-similar; in this case the bow shock can be described as a coordinate surface with $\eta = \eta_b$ for all times. This is achieved by setting $c = c_o L_b$, where c_o is a constant and $L_b = f(t)$ is the ‘length’ of the bow shock as described above (see Appendix A.1.2). It follows that

$$\begin{aligned} c_o L_b c_r \left(\frac{\partial}{\partial t} \mathbf{v}' + \dot{\eta} \frac{\partial}{\partial \eta} \mathbf{v}' + \dot{\xi} \frac{\partial}{\partial \xi} \mathbf{v}' \right) \\ + (\mathbf{v}' \cdot \nabla') \mathbf{v}' &= -\frac{1}{\rho'} \nabla' p', \\ c_o L_b c_r \left(\frac{\partial}{\partial t} \rho' + \dot{\eta} \frac{\partial}{\partial \eta} \rho' + \dot{\xi} \frac{\partial}{\partial \xi} \rho' \right) \\ + \nabla' \cdot (\rho' \mathbf{v}') &= 0, \\ c_o L_b c_r \left(\frac{\partial}{\partial t} \frac{p'}{\rho'^\Gamma} + \dot{\eta} \frac{\partial}{\partial \eta} \frac{p'}{\rho'^\Gamma} + \dot{\xi} \frac{\partial}{\partial \xi} \frac{p'}{\rho'^\Gamma} \right) \\ + (\mathbf{v}' \cdot \nabla') \frac{p'}{\rho'^\Gamma} &= 0. \end{aligned} \quad (5)$$

Because of the self-similar evolution of both the bow shock and the cocoon the flow between them must also be self-similar. This allows a further simplification of equations (5) by introducing dimensionless variables for the velocity, density and pressure of the shocked IGM in which the dependencies on time (i.e. on L_b and \dot{L}_b) and the spatial coordinates are separated,

$$\begin{aligned}
 \mathbf{v}' &= \dot{L}_b [U_\eta(\eta, \xi) \hat{\mathbf{e}}_\eta + U_\xi(\eta, \xi) \hat{\mathbf{e}}_\xi], \\
 \rho' &= \rho_o \left(\frac{L_b}{a_o}\right)^{-\beta} R(\eta, \xi), \\
 p' &= \rho_o \left(\frac{L_b}{a_o}\right)^{-\beta} \dot{L}_b^2 P(\eta, \xi),
 \end{aligned} \tag{6}$$

where we model the external density distribution with a power law, $\rho_o(r/a_o)^{-\beta}$ with ρ_o the central density, a_o the core radius and r the radial distance from the centre of the distribution.

Using the comoving coordinate system described above and replacing the flow variables with their dimensionless counterparts we find

$$\begin{aligned}
 c_o c_r \frac{\ddot{L}_b L_b}{\dot{L}_b^2} U_\eta + b_\eta \frac{\partial}{\partial \eta} U_\eta + b_\xi \frac{\partial}{\partial \xi} U_\eta \\
 + (c_g U_\eta - c_e U_\xi - 2 c_o c_r c_e c_g) U_\xi + \frac{1}{R} \frac{\partial}{\partial \eta} P &= 0, \\
 c_o c_r \frac{\ddot{L}_b L_b}{\dot{L}_b^2} U_\xi + b_\eta \frac{\partial}{\partial \eta} U_\xi + b_\xi \frac{\partial}{\partial \xi} U_\xi \\
 - (c_g U_\eta - c_e U_\xi - 2 c_o c_r c_e c_g) U_\eta + \frac{1}{R} \frac{\partial}{\partial \xi} P &= 0, \\
 R \frac{\partial}{\partial \eta} U_\eta + b_\eta \frac{\partial}{\partial \eta} R + R \frac{\partial}{\partial \xi} U_\xi + b_\xi \frac{\partial}{\partial \xi} R \\
 + [(c_e + \coth \eta) U_\eta + (c_g + \cot \xi) U_\xi - c_o c_r \beta] R &= 0, \\
 - \frac{\Gamma P b_\eta}{R} \frac{\partial}{\partial \eta} R + b_\eta \frac{\partial}{\partial \eta} P - \frac{\Gamma P b_\xi}{R} \frac{\partial}{\partial \xi} R \\
 + b_\xi \frac{\partial}{\partial \xi} P + c_o c_r \left[(\Gamma - 1) \beta + 2 \frac{\ddot{L}_b L_b}{\dot{L}_b^2} \right] P &= 0, \tag{7}
 \end{aligned}$$

where we have split the equation of motion into two equations corresponding to components parallel to $\hat{\mathbf{e}}_\eta$ and $\hat{\mathbf{e}}_\xi$ respectively, and

$$b_\eta = U_\eta - c_o c_r c_e, \quad b_\xi = U_\xi + c_o c_r c_g. \tag{8}$$

Furthermore, the ratio of the length of the bow shock, L_b , and the length of the cocoon, L_c , must also be a constant. Using the result

$$L_c = c_1 \left(\rho_o a_o^\beta\right)^{-\frac{1}{5-\beta}} Q_o^{\frac{1}{5-\beta}} t^{\frac{3}{5-\beta}} \tag{9}$$

from KA, where Q_o is the jet power and c_1 is a dimensionless constant, $\ddot{L}_b L_b / \dot{L}_b^2$ reduces to $(\beta - 2)/3$, and the time dependence in equations (7) can be eliminated.

3 NUMERICAL METHOD

The set of equations (7) represent a system of first order partial differential equations. Although there are no time derivatives in this set the general form is that of an initial value problem because the values of the variables are known at the surface of the bow shock and the solution has to be propagated from this surface at η_b inwards to smaller η

in the direction of the contact discontinuity delineating the cocoon.

The projection of the bow shock onto the xz -plane is an ellipse with $\eta_b = \text{constant}$ and is described by

$$r_b = \pm \sqrt{c_o \sinh^2 \eta_b + \tanh^2 \eta_b l_b^2}, \tag{10}$$

where l_b is the dimensionless coordinate defined by $l_b = z/L_b$. At the tip of the bow shock where $l_b = 1$, $r_b = 0$, and for $l_b = 1/2$ one finds $r_b = 1/(2 R_b)$. These conditions yield

$$c_o = \sqrt{1 - \frac{1}{3 R_b^2}}, \quad \cosh \eta_b = \frac{1}{c_o}. \tag{11}$$

To derive the initial conditions at the bow shock we need to know the velocity of the bow shock perpendicular to its surface, v_\perp , and from the appendix of KA we find

$$v_\perp = \frac{v_x - \frac{\partial r_b}{\partial z} v_z}{\sqrt{\left(\frac{\partial r_b}{\partial z}\right)^2 + 1}}. \tag{12}$$

Since the bow shock expands self-similarly, $v_x = x/L_b$ and $v_z = l_b$. By assuming that the bow shock is strong and that the adiabatic index of the external atmosphere is 5/3 this implies for the assumed elliptical shape of the shock surface

$$\begin{aligned}
 U_\eta(\eta_b, \xi) &= \frac{3}{4} \frac{\sinh \eta_b}{c_r}, \\
 U_\xi(\eta_b, \xi) &= 0, \\
 R(\eta_b, \xi) &= 4 c_o^{-\beta} (\cos^2 \xi + \sinh^2 \eta_b)^{-\frac{\beta}{2}}, \\
 P(\eta_b, \xi) &= \frac{3}{4} c_o^{-\beta} (\cos^2 \xi + \sinh^2 \eta_b)^{-\frac{\beta}{2}} \frac{\sinh^2 \eta_b}{c_r^2}.
 \end{aligned} \tag{13}$$

Given the symmetry of the problem it is sufficient to integrate the equations only between $\xi = 0$ and $\xi = \pi/2$ which corresponds to the z and x -axes respectively, and the following boundary conditions must apply along these coordinate lines:

$$\begin{aligned}
 U_\xi &= 0, \\
 \frac{\partial}{\partial \xi} U_\eta &= 0, \\
 \frac{\partial}{\partial \xi} R &= 0, \\
 \frac{\partial}{\partial \xi} P &= 0.
 \end{aligned} \tag{14}$$

The numerical integration was performed using a finite difference discretisation scheme employing NAG[†] routines on a grid of 1001 points between $\xi = 0$ and $\xi = \pi/2$ separated by equal intervals of length $\pi/2000$. Equations (7) are non-linear and it is therefore not straightforward to assess the stability of the numerical method used. Trial calculations show that in particular the solution for U_ξ is subject to oscillations. To suppress these oscillations, it is necessary to introduce an ‘artificial viscosity’ term of the form $a \partial^2 U_\xi / \partial \xi^2$ to all equations in the system containing expressions proportional to $\partial U_\xi / \partial \xi$ (e.g. Richtmyer & Morton

[†] NAG is a registered trademark of Numerical Algorithms Group Ltd.

1967). The constant a is chosen to be small compared to any other term in the system of equations in order to keep the influence of the ‘artificial viscosity’ within the error of the integration method.

The integration has to be stopped at the contact discontinuity. There can be no gas flow across this surface and therefore the criterion for stopping the integration is met when the component of the gas velocity perpendicular to the contact discontinuity is equal to the corresponding component of the self-similar expansion velocity of this surface. The shape of the contact surface, $r_c(z)$, and therefore the self-similar expansion velocity, $z \hat{e}_z + r_c(z) \hat{e}_x$, is not known *a priori*. Since the bow shock will be closest to the cocoon at the hot spot, one expects the flow to first reach the expansion velocity of the cocoon at $\xi = 0$ and some value $\eta = \eta_c$, i.e. on the z -axis. Assuming that $\partial r_c / \partial z \rightarrow \infty$ at this point, the condition for stopping the integration on the z -axis becomes $U_\eta(\eta_c, \xi = 0) = c_o \cosh \eta_c$, where we have again made use of the fact that the cocoon is expanding self-similarly. A comparison with equation (8) shows that at this point $b_\eta = 0$ which means that the system of equations (7) breaks down, as one would expect at a contact discontinuity.

The integration was advanced from the bow shock at $\eta = \eta_b$ to smaller values of η in steps of $\eta_b/5 \times 10^4$ and after each step it was checked whether the flow had reached the cocoon at the hot spot, i.e. whether the velocity of the flow along the z -axis was within 1% of the self-similar velocity.

The cocoon is not elliptical and therefore does not coincide with the coordinate surface at η_c . The integration was continued by considering the grid point of the finite difference mesh of smallest ξ for which the solution had not yet reached the contact surface. All derivatives with respect to ξ in equations (7) were approximated by linear extrapolation using two values of these expressions separated by $\eta_b/5 \times 10^2$ along a line of constant ξ . This extrapolation effectively converts equations (7) into a system of ordinary differential equations which were solved using an implementation of the backward differentiation formulae from the NAG[†] library. The integration was continued until the solution for the last point of the grid had reached the cocoon.

4 THE GAS FLOW BETWEEN BOW SHOCK AND COCOON

An important test of the analysis and integration presented here is to consider the case of a spherical symmetric wind as discussed by Dyson *et al.* (1980). These authors considered only the case of a wind expanding into a uniform atmosphere, but using the results of the previous section it is straightforward to extend their analysis to more complex environments in which $\beta \neq 0$ (for a solution using King density profiles see Heinz *et al.* 1998).

In the case of a spherical bow shock there is an additional degree of rotational symmetry about the x -axis. This implies that one can set $\xi = 0$; U_ξ and all derivatives with respect to ξ vanish. Furthermore it is possible to change from the remaining prolate spheroidal coordinate η to the more familiar spherical polar coordinate r by using $r = c_o \cosh \eta$. Because of these simplifications the second equation in (7) vanishes completely and we obtain

$$\begin{aligned} \frac{\beta - 2}{3} U_r + (U_r - r) \frac{\partial}{\partial r} U_r + \frac{1}{R} \frac{\partial}{\partial r} P &= 0, \\ R \frac{\partial}{\partial r} U_r + (U_r - r) \frac{\partial}{\partial r} R + 2 \frac{U_r R}{r} - \beta R &= 0, \\ -\frac{\Gamma P}{R} (U_r - r) \frac{\partial}{\partial r} R + (U_r - r) \frac{\partial}{\partial r} P \\ + \frac{3\Gamma\beta - \beta - 4}{3} P &= 0, \end{aligned} \quad (15)$$

where we have used $R_b = 1/\sqrt{3}$ for a spherical bow shock and therefore $\eta_b \rightarrow \infty$ which implies that $\coth \eta \rightarrow 1$ for all η close to η_b . Setting $\beta = 0$ recovers the equations used by Dyson *et al.* (1980). The initial conditions at the bow shock at $r = 1$ for the spherical case are $U_r = 3/4$, $R = 4$ and $P = 3/4$.

Figure 4 shows plots of the solution for the case of a spherical bow shock. The curves for $\beta = 0$ are identical to those presented by Dyson *et al.* (1980). In this case the contact discontinuity is reached at $r_c = 0.86$. For the two other cases presented here we find $r_c = 0.85$ and $r_c = 0.84$ for $\beta = 1$ and $\beta = 2$ respectively. In all three cases the gas is accelerated away from the cocoon but the acceleration is somewhat less effective for the cases with a density gradient in the external atmosphere, hence the greater detachment of the cocoon from the bow shock. While this difference in the flow pattern is not very significant, the distribution of the density and the pressure of the gas behind the bow shock is distinctively different for each case. The gas is expanding adiabatically after being compressed by the bow shock. This behaviour is evident from the curves in Figure 4 for $\beta = 0$ but is masked for $\beta = 2$ by the presence of dense gas at high pressure close to the cocoon which has passed through the bow shock earlier than the material in the regions closer to the bow shock. The density and pressure of the external gas in front of the bow shock decreases faster than that of the material which is expanding after passing through the bow shock, giving the impression that the gas is further compressed after passing through the bow shock. In this case the cocoon is surrounded by a relatively thin, heavy shell of highly compressed gas, while for $\beta = 0$ the gas closest to the contact discontinuity is rarefied.

Results from the numerical integrations of equations (7) for the more complicated case of ellipsoidal bow shocks applicable to FR II sources are summarized in Table 4. Note, that the stand-off distances between bow shock and cocoon are small both at the hot spot and close to the x -axis. The shape of the cocoon is therefore also close to an ellipsoid and this agrees well with observations (e.g. Leahy & Williams, 1984). The following sections describe the results in greater detail.

4.1 The velocity field

Figure 4.1 shows a cut defined by the xz -plane of the velocity field of the gas flow between bow shock and contact discontinuity for one half of a wide ($R_b = 1$) ellipsoidal bow shock in a uniform atmosphere. Because of the rotational symmetry about the z -axis the vectors are lying fully in the xz -plane and there is a reflection symmetry about the z -axis. The vectors show the velocity of the flow with respect

to the comoving coordinate system, with the bow shock and cocoon at rest.

A closer examination of the flow close to the hot spot shows the flow bending around the tip of the cocoon and then moving along the contact discontinuity (Figure 4.1, left). On the z -axis, the axis of the jet, the flow ends in a stagnation point at the hot spot, similar to the case of a spherical bow shock. Close to the x -axis the flow is decelerated and there is a stagnation point on the x -axis ahead of the cocoon (Figure 4.1, right). This behaviour is imposed on the solution by the assumed symmetry. The flow pattern is very similar for other values of β and R_b .

4.2 Density and pressure

The density distribution associated with the flow is shown in Figure 4.2. For a uniform atmosphere the density of the shocked gas decreases towards the cocoon to a value which is below that of the external density, similar to the behaviour of the gas behind a spherical bow shock. For $\beta = 1$ the density decreases slowly from the bow shock to the cocoon, again similar to the spherical case (Figure 4), however, the density of the gas just behind the shock now decreases monotonically with increasing x because of the external density gradient. For $\beta = 2$ a similar trend with increasing x is seen, together with an increase in density from the bow shock to the cocoon.

The pressure distribution of the gas between bow shock and contact discontinuity is shown in Figure 4.2. For a uniform external density the pressure decreases monotonically from the hot spot towards the x -axis, whereas for a decreasing density profile the pressure firstly decreases away from the hot spot then increases again towards the x -axis. For $\beta = 2$ the pressure close to the x -axis almost reaches the pressure in front of the hot spot.

In the analysis presented in KA which led to the prediction of self-similar expansion of bow shock and cocoon we showed that it is a good approximation to assume a constant pressure distribution within the cocoon due to a high sound speed in this region. Across the contact surface pressure is of course continuous. The results shown in Figure 4.2 indicate a pressure variation around the contact surface which is a minimum at some point between the hot spot and the x -axis. In fact, within the cocoon there must be a backflow (e.g. Norman *et al.* 1982) which is initially accelerated from the hot spot and must, given the assumed symmetry, be decelerated towards the symmetry plane of the x -axis. For most values of β this pressure variation is small and therefore we believe the expansion of the source will remain approximately self-similar and the results of KA and the analysis presented here will apply. For β close to 2 the pressure variation becomes significant. The solution presented here will then be valid while the source has an approximately elliptical shape, however in this case the source is unlikely to expand self-similarly. This is because one of the assumptions for self-similarity is the pressure equilibrium of the jets within the radio cocoon the pressure within which is assume to be uniform away from the hot spots. At least two possibilities for the evolution of such a source exist. Firstly,

if the source retains approximate axial symmetry then as the high sound speed in the cocoon leads to pressure equalization, the excess pressure in the shocked gas will cause the cocoon to collapse resulting in a ‘pinching off’ of the cocoon; the bow shock will then not follow an elliptical coordinate surface, although subsequent expansion may still be approximately self-similar. Alternatively, the axial symmetry of the problem may not be retained leading to significant off-axis flow in the cocoon as is commonly observed.

Note also that with the steeper rise of the pressure in direction of the core for large β the density is increasing as well in these regions. This implies that radiative cooling due to thermal bremsstrahlung becomes important and our assumption of adiabatic conditions may not be valid at this point. Any cooling will decrease the pressure and including radiative processes in the analysis should alleviate the problem of the steep pressure gradients towards the core. However, including these effects is beyond the scope of this paper and in the present form the existence of the pressure gradients described above means that the model is not fully self-consistent for large values of β .

A comparison of the density and pressure distributions for different aspect ratios of the bow shock but for the same external atmosphere is shown in Figure 4.2. The gradients in the density and the pressure distribution are greater for higher R_b . The variation in pressure is again seen to be smaller than in density. The stand-off distance between bow shock and cocoon at the hot spot, Δ_h , decreases for increasing R_b , while it stays almost constant for constant R_b but increasing β (see Table 4). For large values of R_b the stand-off distance at the x -axis, Δ_x , decreases with increasing β .

We conclude that for β somewhat less than 2 self-similar expansion can occur with a flow distribution and source shape well approximated by the analysis presented here. For β close to 2 the source may pass through a phase in which the analysis of the present paper applies, but this does not represent a self-similar expansion and deviations from the assumptions of axial symmetry or elliptical bow shocks must occur.

4.3 Confinement of the cocoon

In our analysis presented in KA the ratio of the pressure at the hot spot, p_h , and that of the cocoon, p_c , determines the value of the dimensionless constant c_1 which describes the expansion of the cocoon. In the case of a cylindrical cocoon which is confined by the ram pressure of the receding IGM a simple estimate gives

$$\frac{p_h}{p_c} = 4 R^2. \quad (16)$$

This estimate ignores the variation in external density along the outside of the cocoon and the small amount of backflow. Taking p_c to be the pressure at the contact discontinuity half way between the core and the hot spot, we find that our results are well fitted by empirical relations of the form

$$\frac{p_h}{p_c} = \begin{cases} 2.51 R^{1.95} & ; \beta = 0 \\ 1.95 R^{1.63} & ; \beta = 1 \\ 1.03 R^{1.57} & ; \beta = 2 \end{cases}. \quad (17)$$

The assumption of ram pressure confinement of the cocoon, equation (16), therefore leads to an overestimate of the ratio p_h/p_c .

Because of the self-similar expansion of the cocoons, the cocoon volume is given as $c_3 L_c^3$, where L_c is the length of the cocoon and c_3 is a constant depending on the cocoon geometry. The values of c_3 derived from the analysis presented here are given in Table 4. For the assumption of a cylindrical cocoon c_3 equals $\pi/(4R^2)$; we find a maximal deviation of only 28% of this approximation from our results.

The profile of the density distribution in the environments of extragalactic radio sources is well fitted by a King (1972) profile. For distances from the centre of the density distribution greater than the core radius, a_o , the King profile is well fitted by the power law distribution, and for distances smaller than a_o a constant density ρ_o is a good approximation. Consider a radio source which starts out in such a uniform density environment and expands beyond the core radius. KA argue that the ratio p_h/p_c is determined by intrinsic properties of the jet since the cocoon and the jet are assumed to be in pressure balance. In this case equations (17) imply that the cocoon of such a source will become narrower when it emerges from the uniform density regime into the region with a decreasing density gradient. This result is in agreement with the observation of Black (1992) who notes that in his sample shorter sources tend to be ‘fatter’.

5 X-RAY EMISSION FROM THE HEATED IGM

Assuming the shocked IGM between bow shock and contact discontinuity is an ideal gas consisting entirely of ionised hydrogen the absolute temperature at any given point in the flow is

$$T = \frac{m_p}{k} \dot{L}_b^2 \frac{P(\eta, \xi)}{R(\eta, \xi)}, \quad (18)$$

where m_p is the mass of a proton and k is the Boltzmann constant. Note, that the temperature of the gas in the flow does not depend on the temperature of the environment the source is expanding into.

Figure 5 shows a plot of the ratio P/R for various atmospheres. The differences between the temperature distribution for different β are relatively small. The thin shell of rarefied gas around the cocoon in a uniform atmosphere is slightly hotter than its surroundings and the overall temperature of the gas in the flow decreases somewhat for increasing β . A comparison of models for various aspect ratios (Figure 5, left column) shows an increasing prominence of the hot spot region with increasing R_b which can be explained by the faster expansion speed of the bow shock at the hot spot with respect to the expansion perpendicular to the jet axis. Again the temperature scale is very similar in all four panels.

The specific emissivity of ionised hydrogen at temperature T due to thermal Bremsstrahlung is (e.g. Shu, 1991)

$$\epsilon_\nu = 7 \times 10^{-51} \frac{n_e n_p}{\sqrt{T}} e^{-\frac{h\nu}{kT}} \frac{W}{\text{m}^3 \text{Hz}}, \quad (19)$$

where n_e and n_p are the number densities of the electrons and of the protons respectively. When observed with a finite bandwidth, $\nu_1 \rightarrow \nu_2$, the integrated X-ray emissivity is given by

$$\epsilon = 5.6 \times 10^{11} \frac{(\rho_o a_o^\beta)^2}{a_1} L_b^{\frac{-5\beta-2}{3}} \sqrt{R^3 P} \times \left[e^{-4.0 \times 10^{-7} a_1^2 L_b^{\frac{4-2\beta}{3}} \nu \frac{R}{P}} \right]_{\nu_2}^{\nu_1} \frac{W}{\text{m}^3}, \quad (20)$$

with

$$a_1 \equiv \frac{5-\beta}{3} c_1^{\frac{\beta-5}{3}} (\rho_o a_o^\beta)^{\frac{1}{3}} Q_o^{-\frac{1}{3}}, \quad (21)$$

where we have used equation (9). To obtain the X-ray surface brightness this expression has to be integrated along the line of sight through the flow. The dependence of ϵ on the advance speed of the bow shock, \dot{L}_b , is non-linear. To proceed we therefore have to choose specific values for the external density profile, the jet power, the linear size of the cocoon, L_j and the observing frequency. Assuming $\rho_o = 5 \times 10^{-22} \text{ kg/m}^3$, $a_o = 1 \text{ kpc}$, typical values for the gas surrounding isolated galaxies (Canizares *et al.* 1987), $Q_o = 10^{39} \text{ W}$ (Rawlings & Saunders 1991), $L_j = 100 \text{ kpc}$ and an observing band from $\nu_1 = 0.1 \text{ keV}$ to $\nu_2 = 2 \text{ keV}$ (appropriate for the High Resolution Imager, *HRI*, of the *ROSAT* satellite) we obtain the results shown in Figure 5. Here we have assumed that the source is rotationally symmetric about the z -axis, that the source lies exactly in the plane of the sky and we have neglected the cosmological redshift of the observing frequency.

The appearance of the flow in X-ray emission varies significantly with β . For a uniform density environment the hot spot region dominates the emission, while for higher values of β the region close to the x -axis is brightest and the emission is concentrated towards the edge of the cocoon. Together with the observation made earlier that the temperature variation is not very large within the flow it is now evident that the X-ray surface brightness for the frequency band chosen is a good tracer of the density distribution. X-ray observations of FR II sources with high resolution can therefore constrain the shape of the density distribution of the atmosphere the source is expanding into. A similar result was found by Clarke *et al.* (1997) from numerical simulations of a cocoon-bow shock structure around a jet. For smaller aspect ratios the X-ray surface brightness is more diffuse (see Figure 5, right column), but the general features of the appearance of the source remain the same. Note however the difference in the ages of the sources of the same linear size but of different geometry and/or environment.

Heinz *et al.* (1998) introduce observational diagnostics for X-ray observations of extragalactic radio sources. These are based on their assumption of spherical geometry for the bow shock and cocoon which implies a uniform surface brightness at all points within the flow at equal distance from the centre of the source. From the analysis presented here it is clear that the X-ray surface brightness of the flow between bow shock and cocoon can vary considerably within the flow region if the source geometry is elongated and/or

the density gradient of the external medium is steep. In these cases it is not straightforward to infer the absolute values of source or environment parameters from X-ray observations alone.

The total radiation due to thermal bremsstrahlung, dE/dt , can be found by setting $\nu_1 = 0$ and $\nu_2 \rightarrow \infty$ in equation (20) and integrating the resulting emissivity over the volume of the flow. For almost all the cases investigated here we find the total luminosity to be significantly less than 10% of the jet power. We therefore conclude that our adiabatic treatment of the flow between bow shock and cocoon is justified.

A rough estimate for the local cooling time of the shocked IGM can be obtained by dividing the local energy density, $P(\eta, \xi)$, by dE/dt . For all cases presented in this paper we find cooling times of the order of 10% to a few thousand times the Hubble time which is much greater than the inferred life times of radio sources. The presence of a radio source therefore influences the evolution of its environment far beyond the limited life time of the source itself.

5.1 Application of the model to Cygnus A and 3C 356

The high resolution *ROSAT* map of Carilli *et al.* (1994) has sufficient spatial resolution to allow a comparison of source features observed in the radio at low frequency with those observed in X-rays. For the density distribution of the material surrounding Cygnus A we find $\rho_o = 1.4 \times 10^{-22} \text{ kg/m}^3$, $a_o = 25.6 \text{ kpc}$ and $\beta = 1.4$ from the fitting of the X-ray surface brightness distribution expected from a King profile ($\Omega = 1$, $H_o = 50 \text{ km s}^{-1} \text{ Mpc}^{-1}$) to the data presented by Carilli *et al.* (1994). Note, that this is different from the fit obtained by these authors. Arnaud *et al.* (1987) determine the temperature of the gas to be $4 \times 10^7 \text{ K}$. Carilli *et al.* (1994) also present a 347 MHz VLA map of Cygnus A from which it is possible to determine the linear size and the aspect ratio of the cocoon. Assuming that Cygnus A is lying exactly in the plane of the sky we find $L_j \approx 105 \text{ kpc}$ and $R \approx 2$; the difference in the lengths of the two cocoons is roughly 15%. The results of an integration of the hydrodynamical equations describing the flow between bow shock and cocoon for these parameters is given in Table 4. The aspect ratio of the bow shock of Cygnus A implied by this calculation is 1.6.

Using the model of Kaiser, Dennett-Thorpe & Alexander (1997) for the radio emission of FR II sources we have calculated the radio spectrum of Cygnus A for the given parameters. The model is in good agreement with the observed radio luminosities in the Gigahertz range presented by Baars *et al.* (1977) for a jet power of $Q_o = 2 \times 10^{39} \text{ W}$. Using the value of $p_h/p_c = 4.1$ and the model of KA we find an age of 2.9×10^7 years for Cygnus A. The present hot spot advance speed implied by this is $9.7 \times 10^{-3} c$. Both results agree well with those of Carilli *et al.* (1991).

After subtracting the expected X-ray emission due to thermal bremsstrahlung of a King profile with the parameters quoted from the map presented by Carilli *et al.* (1994), the excess or deficit of the emission due to the presence of the

radio source becomes visible. The most interesting feature for this analysis are the emission enhancements to the sides and just outside the cocoons because they must be caused by the shocked IGM between bow shock and cocoon. For the eastern cocoon the peak in the residual emission lies towards the core of the radio structure and the excess measured after the King profile has been subtracted is 0.21 counts per second per 0.5 arcsecond pixel with the *HRI* in the band between 0.1 keV and 2 keV. This implies an X-ray emission of the gas in this region corresponding to 0.27 counts per second per pixel with the *HRI* because the measured count rate along a line of sight through the cocoon region, which we assume to be free of X-ray emitting gas, is 0.06 counts per second per pixel less than that expected from the King profile. For the western cocoon the situation is less clear and the emission enhancement may not be significant.

The surface brightness map for the case of Cygnus A is very similar to the one shown on the bottom right of Figure 5. Qualitatively the predictions of the numerical calculation presented here agree well with the observations. The emission enhancements are at the correct positions, close to the core of the source just outside the cocoon. However, a closer examination of the temperature distribution reveals some severe problems with the application of the results found in the previous section to the case of Cygnus A. The value of P/R at the point of highest surface brightness is roughly 0.012. Together with the derived advance speed of the hot spot we find a temperature of $1.9 \times 10^6 \text{ K}$ at this point. This is well below the temperature of the King profile assumed for the gas which surrounds the bow shock. Indeed, even the model temperature just behind the bow shock close to the core of the source is below the temperature of the unshocked gas. This is caused by the assumption of strong shock conditions along the entire bow shock which may not be applicable to the case of Cygnus A.

Using the temperature of the ambient gas the peak in the X-ray surface brightness predicted by our model is $4 \times 10^{-16} \text{ W m}^{-2}$ per 0.5 arcsecond pixel which corresponds to 0.012 counts per second per pixel with the *HRI*. For the conversion we have used the Internet version of PIMMS[‡] with a column density for the galactic medium of $3 \times 10^{25} \text{ m}^{-2}$ towards Cygnus A (Clarke *et al.* 1997). This discrepancy may be explained by the existence of cold, dense clumps of gas embedded in the otherwise smooth distribution of gas in galaxy clusters (Fabian *et al.* 1994). The X-ray emission of a volume of gas after the bow shock has passed through it is proportional to $\rho^2 M \sqrt{T}$, where ρ is the pre-shock density of the gas, M the Mach number of the shock within the gas and T the temperature. For ideal gas conditions the Mach number is proportional to v/\sqrt{T} , where v is the velocity of the shock with respect to the gas. The ratio of the X-ray luminosity of a cold, dense cloud and that of hot IGM with the same volume is then given by $\rho_c^2 v_c / (\rho_x^2 v_x)$, where subscripts c and x are used for the cloud material and the hot IGM respectively. The cold clouds are small and

[‡] PIMMS was programmed by K. Mukai at the High Energy Astrophysics Science Archive Research Center of NASA, available at <http://heasarc.gsfc.nasa.gov/Tools/w3pimms.html>

will therefore quickly re-establish pressure equilibrium with the shocked hot IGM surrounding it after the bow shock has passed through it (e.g. McKee & Cowie 1975). We can therefore set the velocity of the bow shock within the cloud material to $\sim \sqrt{\rho_x/\rho_c v_x}$. With this we find that the ratio of the X-ray luminosity of a cold cloud and that of the hot IGM occupying the same volume is given by $(\rho_c/\rho_x)^{3/2}$. The peak in the X-ray emission observed in the eastern lobe of Cygnus A can thus be explained if the gas in this region is about 5 times denser than the otherwise smoothly distributed IGM.

The striking symmetry of the two emission peaks on either side of the base of the eastern cocoon is difficult to explain in this scenario. Note however, that there is another peak in the X-ray emission situated to the south-west of the core well inside the western cocoon. This could be another clump of cold material with similar properties to the two discussed above, which is observed in projection and therefore appears to lie within the cocoon.

Crawford & Fabian (1996) report the detection of extended X-ray emission in the vicinity of the FR II radio galaxy 3C 356. They argue that the emission is the signature of an extended IGM in a cluster around 3C 356 which makes this radio galaxy the most distant object ($z=1.079$) in which cluster gas has been detected directly. The resolution of the X-ray map of this object is insufficient for any quantitative study. However, the observed extension is aligned with the northern cocoon of 3C356 which suggests that the X-ray emission of the IGM surrounding the northern cocoon may be enhanced by the compression and heating of this material by the bow shock of the radio source, similar to the case of Cygnus A.

5.2 An empirical model for the X-ray emission

It is straightforward to calculate the total X-ray luminosity of the shocked IGM between the bow shock and the cocoon for a given frequency and bandwidth, L_X , predicted by the model for a given set of source parameters by integrating over the surface area of the bow shock. However, this requires the numerical calculation to be performed for this particular set of parameters. In the following we develop an analytical approximation for the X-ray luminosity using empirical relations of source parameters derived from the numerical calculations.

The total mass of the external gas swept up by the bow shock during the life time of the radio source, M , is given by

$$M = \int \rho_o \left(\frac{r}{a_o}\right)^{-\beta} dV_b = 4\pi \rho_o a_o^\beta L_b^{3-\beta} I, \quad (22)$$

where

$$I \equiv \int_0^{\pi/2} \int_0^{\eta_b} \sinh \eta \sin \xi \frac{\sinh^2 \eta + \sin^2 \xi}{(\cos^2 \xi + \sinh^2 \eta)} d\xi d\eta. \quad (23)$$

If we assume this mass to be uniformly distributed over the volume occupied by the flow, the density in this region is found to be $\bar{\rho} = M/(V_b - V_c) \equiv M/(a_2 L_b^3)$, where V_b and V_c are the volume enclosed by the bow

shock and that of the cocoon respectively. By definition $V_b = 2\pi L_b^3 (c_o^2 \sinh^2 \eta_b - 1/3 \tanh^2 \eta_b)$ and $V_c = c_3 L_b^3$.

We define \bar{T} as the average of the temperature of the gas in the flow and since the temperature variations within the flow material are small, local deviations from \bar{T} will be small as well. For an ideal gas $\bar{T} = m_p/k \dot{L}_b^2 P/R$.

With the two assumptions of uniform density and uniform temperature in the flow we find from equation (19)

$$\begin{aligned} \bar{L}_X &= 5.2 \times 10^{13} \bar{\rho} \sqrt{\bar{T}} (V_b - V_c) \left[e^{-4.8 \times 10^{-11} \nu/\bar{T}} \right]_{\nu_2}^{\nu_1} \\ &= 9.1 \times 10^{13} \frac{I^2}{a_2} \frac{(\rho_o a_o^\beta)^2}{a_1} L_b^{\frac{7-5\beta}{3}} \sqrt{P/R} \\ &\times \left[e^{-4.0 \times 10^{-7} a_1^2 L_b^{\frac{4-2\beta}{3}} 1/P/R} \right]_{\nu_2}^{\nu_1}. \end{aligned} \quad (24)$$

This expression depends on c_1 , $\overline{P/R}$ and I/a_2 which are all functions of the exponent of the density profile of the unshocked IGM, β , and the geometry of the FR II source defined by the aspect ratios R or R_b . Empirical expressions for these functions can be derived from the results of the numerical calculation. We find

$$\begin{aligned} \overline{P/R} &= \begin{cases} 0.17 R^{-1.60} & \text{or } 0.12 R_b^{-1.74} & ; \beta = 0 \\ 0.13 R^{-1.68} & \text{or } 0.088 R_b^{-1.71} & ; \beta = 1 \\ 0.095 R^{-1.67} & \text{or } 0.068 R_b^{-1.64} & ; \beta = 2 \end{cases}, \\ I/a_2 &= \begin{cases} 0.029 R^{-1.89} & \text{or } 0.019 R_b^{-2.05} & ; \beta = 0 \\ 0.12 R^{-1.00} & \text{or } 0.093 R_b^{-1.01} & ; \beta = 1 \\ 0.75 R^{0.50} & \text{or } 0.83 R_b^{0.49} & ; \beta = 2 \end{cases}, \\ c_1 &= \begin{cases} 1.22 R^{0.49} & \text{or } 1.35 R_b^{0.53} & ; \beta = 0 \\ 1.02 R^{0.63} & \text{or } 1.18 R_b^{0.64} & ; \beta = 1 \\ 0.71 R^{0.88} & \text{or } 0.85 R_b^{0.86} & ; \beta = 2 \end{cases} \end{aligned} \quad (25)$$

Figure 5.2 shows a comparison of equation (24) using the empirical relations above, with the results of the numerical calculation for $\rho_o = 5 \times 10^{-22} \text{ kg m}^{-3}$, $a_o = 1 \text{ kpc}$, $Q_o = 10^{39} \text{ W}$, $\nu_1 = 0.1 \text{ keV}$ and $\nu_2 = 2 \text{ keV}$. For $\beta > 0$ the empirical model agrees well with the numerical results. The deviation for large linear sizes and $\beta = 0$ is acceptable in many cases since it is unlikely that a uniform density region extends to very large distance from the centre of any object hosting a radio source. Note however, that the fit of the empirical model worsens for higher observing frequencies since the exponential part of equation (20), which is not well fitted by the empirical formula, then dominates this expression.

6 CONCLUSIONS

We presented a numerical integration of the hydrodynamical equations governing the self-similar gas flow behind a strong shock in two dimensions assuming the shock to have an ellipsoidal geometry. The density distribution in the unshocked environment of the shock is modeled with a power law. Applying this model to the bow shocks surrounding the cocoons of extragalactic radio sources we found that there should be a pressure gradient within the cocoons of sources located in

non-uniform environments which is consistent with the existence of backflow within the cocoon. In extreme density profiles non-axially symmetric flow or pinching-off of the cocoon is very likely to occur. Furthermore, the expansion of the cocoon and bow shock may not be self-similar. In these cases ($\beta \sim 2$) the model is not self-consistent. We also find that the assumption of ram pressure confinement of the cocoon perpendicular to the jet axis leads to an overestimate of the ratio of the pressure in front of the hot spot and the pressure in the cocoon.

From the properties of the gas in the flow we calculated the X-ray surface brightness predicted by the model. Because of the small variations of the temperature in the flow, the surface brightness was found to be a good tracer of the gas density. The appearance of radio sources in X-rays is found to vary significantly with the properties of the external medium. Simple diagnostic tools have to be refined to account for the elongation of the bow shock of most sources. The cooling times of the IGM shocked by the bow shock are much longer than the expected life time of the radio sources causing the bow shock. The evolution of any concentration of matter in the universe will therefore be significantly influenced by the presence of a radio source in its centre. This is the case even if the activity time scale of the source is much shorter than the evolution time scale of its surroundings.

We compared the predictions of our model with the X-ray map of Cygnus A of Carilli *et al.* (1994). Although our model predicts the strongest X-ray emission at the position where it is observed, on the outside of the cocoon closest to the core of the source, the model can not reproduce the observed luminosity. The emission may be caused by the presence of overdense clumps of gas embedded in the otherwise smooth IGM.

The enhanced X-ray emission of the shocked IGM behind the bow shock of a strong radio source may also explain the observed extended X-ray emission around 3C 356.

Based on the numerical calculation we also presented an empirical model for the total X-ray emission expected from the shocked IGM surrounding the cocoons of powerful FR II sources.

Despite the inconsistencies within the model that arise for large values of β we believe that this analysis is an important first step in determining the influence of powerful radio sources on the properties and evolution of their gaseous environments.

ACKNOWLEDGMENTS

The authors thank S. Rawlings for drawing their attention to the X-ray map of 3C 356 and the anonymous referee for her/his very helpful comments.

REFERENCES

Arnaud K. A., Johnstone R. M., Fabian A. C., Crawford C. S., Nulsen P. E., Shafer R. A., Mushotzky R. F., 1987, MNRAS, 227, 241

- Baars J. W. M., Genzel R., Pauliny-Toth I. I. K., Witzel A., 1977, A&A, 61, 99
- Black A. R. S., 1992, PhD thesis, University of Cambridge
- Böhringer H., Voges W., Fabian A. C., Edge A. C., Neumann D. M., 1993, MNRAS, 264, L25
- Canizares C. R., Fabbiano G., Trinchieri G., 1987, ApJ, 312, 503
- Carilli C. L., Perley R. A., Dreher J. W., Leahy J. P., 1991, ApJ, 383, 554
- Carilli C. L., Perley R. A., Harris D. E., 1994, MNRAS, 270, 173
- Clarke D. A., Harris D. E., Carilli C. L., 1997, MNRAS, 284, 981
- Crawford C. S., Fabian A. C., 1996, MNRAS, 281, L5
- Dyson J. E., Falle S. A. E. G., Perry J. J., 1980, MNRAS, 191, 785
- Fabian A. C., Crawford C. S., Edge A. C., Mushotzky R. F., 1994, MNRAS, 267, 779
- Heinz S., Reynolds C. S., Begelman M. C., 1998, ApJ, 501, 126
- Kaiser C. R., Alexander P., 1997, MNRAS, 286, 215, [KA]
- Kaiser C. R., Dennett-Thorpe J., Alexander P., 1997, MNRAS, 292, 723
- King I. R., 1972, ApJ, 174, L123
- Leahy J. P., Williams A. G., 1984, MNRAS, 210, 929
- McKee C. F., Cowie L. L., 1975, ApJ, 195, 715
- Norman M. L., Smarr L., Winkler K.-H. A., Smith M. D., 1982, A&A, 113, 285
- Rawlings S., Saunders R., 1991, Nat., 349, 138
- Rees M. J., 1971, Nat., 229, 312
- Richtmyer R. D., Morton K. W., 1967, Difference methods for initial-value problems. Interscience Publishers
- Scheuer P. A. G., 1974, MNRAS, 166, 513
- Sedov L. I., 1959, Similarity and dimensional methods in mechanics. Academic Press
- Shu F. H., 1991, The physics of astrophysics. Vol.1: Radiation. University Science Books

APPENDIX

A.1 Comoving prolate spheroidal coordinates

A.1.1 Fixed coordinates

The Cartesian coordinates of any point in space can be related to their prolate spheroidal counterparts via the expressions

$$\begin{aligned} z &= c \cosh \eta \cos \xi, \\ x &= c \sinh \eta \sin \xi \sin \phi, \\ y &= c \sinh \eta \sin \xi \cos \phi, \end{aligned} \quad (26)$$

where c is a constant describing the eccentricity of the ellipsoids of constant η (see Figure A.1.1). Since we assume that the bow shock is of ellipsoidal shape with the z -axis, the jet axis, being the axis of rotational symmetry the problem will be independent of ϕ and we seek a solution (without loss of generality) in the xz -plane, i.e. $\phi = \pi/2$. The unit vectors with respect to η and ξ are

$$\begin{aligned} \hat{\mathbf{e}}_\eta &= \frac{1}{c_r} (\sinh \eta \cos \xi \hat{\mathbf{e}}_z + \cosh \eta \sin \xi \hat{\mathbf{e}}_x), \\ \hat{\mathbf{e}}_\xi &= \frac{1}{c_r} (-\cosh \eta \sin \xi \hat{\mathbf{e}}_z + \sinh \eta \cos \xi \hat{\mathbf{e}}_x), \end{aligned} \quad (27)$$

with

$$c_r = \sqrt{\sinh^2 \eta + \sin^2 \xi} \quad (28)$$

It immediately follows that

$$\begin{aligned} \frac{\partial}{\partial \eta} \hat{\mathbf{e}}_\eta &= -c_g \hat{\mathbf{e}}_\xi, & \frac{\partial}{\partial \xi} \hat{\mathbf{e}}_\eta &= c_e \hat{\mathbf{e}}_\xi \\ \frac{\partial}{\partial \xi} \hat{\mathbf{e}}_\xi &= -c_e \hat{\mathbf{e}}_\eta, & \frac{\partial}{\partial \eta} \hat{\mathbf{e}}_\xi &= c_g \hat{\mathbf{e}}_\eta \end{aligned} \quad (29)$$

where

$$\begin{aligned} c_e &= \frac{\sinh \eta \cosh \eta}{c_r^2} \\ c_g &= \frac{\sin \xi \cos \xi}{c_r^2}. \end{aligned} \quad (30)$$

Using equations (26) the η and ξ components of the ∇ -operator in this coordinate system can be found.

$$\begin{aligned} \nabla_\eta &= \frac{1}{c c_r} \frac{\partial}{\partial \eta} \equiv \frac{1}{c c_r} \nabla'_\eta \\ \nabla_\xi &= \frac{1}{c c_r} \frac{\partial}{\partial \xi} \equiv \frac{1}{c c_r} \nabla'_\xi \end{aligned} \quad (31)$$

The divergence of a vector, $\nabla \cdot \mathbf{V}$, in prolate spheroidal coordinates assuming that \mathbf{V} does not depend on ϕ can be written in the form

$$\begin{aligned} c c_r \nabla \cdot \mathbf{V} &= \frac{\partial}{\partial \eta} \mathbf{V}_\eta + (c_e + \coth \eta) \mathbf{V}_\eta \\ &\quad + \frac{\partial}{\partial \xi} \mathbf{V}_\xi + (c_g + \cot \xi) \mathbf{V}_\xi. \end{aligned} \quad (32)$$

A.1.2 Comoving coordinates

By setting $c = c_o L_b$ it is possible to transform the stationary coordinate system discussed in the previous section into comoving coordinates. From equations (26) it is clear that if c is a function of time, η and ξ must also depend on time. Taking the derivative of (26) with respect to t one finds

$$\begin{aligned} \dot{\eta} &= -\frac{\dot{L}_b}{L_b} c_e, \\ \dot{\xi} &= \frac{\dot{L}_b}{L_b} c_g, \end{aligned} \quad (33)$$

where a dot denotes a time derivative. This also means that all partial derivatives with respect to time in equations (4) are replaced according to

$$\frac{\partial}{\partial t} \rightarrow \frac{\partial}{\partial t} + \dot{\eta} \frac{\partial}{\partial \eta} + \dot{\xi} \frac{\partial}{\partial \xi}. \quad (34)$$

Note, that the partial derivatives with respect to the spatial coordinates are unchanged and we therefore continue to use the symbols, η and ξ , for these spatial coordinates.

Table 1. The results of the numerical integration. β is the exponent of the power law for the external density distribution, R_b is the aspect ratio of the bow shock, R is the aspect ratio of the cocoon, p_h/p_c is the ratio of the pressure at the hot spot and the pressure in the cocoon defined as the pressure at the contact discontinuity half way between the core of the radio source and the tip of the cocoon, η_b is the elliptical coordinate surface coinciding with the bow shock, η_h is the elliptical coordinate at which the flow reaches the cocoon in front of the hot spot, η_c is the elliptical coordinate at which the flow reaches the point on the contact discontinuity half way between the core and the tip of the cocoon, η_x is the elliptical coordinate at which the flow reaches the cocoon on the x -axis, Δ_h is the stand-off distance of the bow shock from the contact discontinuity at the hot spot, Δ_x is the stand-off distance of the bow shock from the cocoon at the x -axis and c_3 is the volume constant.

	R_b	R	p_h/p_c	η_b	η_h	η_c	η_x	Δ_h	Δ_x	c_3
$\beta = 0$	1.0	1.221	3.518	0.6585	0.5775	0.5386	0.5373	0.0435	0.1160	0.4153
	2.0	2.679	16.92	0.2971	0.2581	0.2217	0.2217	0.0105	0.0741	0.0940
	3.0	4.125	39.80	0.1949	0.1699	0.1415	0.1415	0.0045	0.0528	0.0403
	4.0	5.559	71.63	0.1454	0.1268	0.1044	0.1044	0.0025	0.0406	0.0223
	5.0	6.985	111.8	0.1160	0.1022	0.0828	0.0828	0.0015	0.0329	0.0146
$\beta = 1$	1.0	1.217	2.384	0.6585	0.5715	0.5386	0.5360	0.0465	0.1172	0.4153
	2.0	2.579	7.973	0.2971	0.2581	0.2300	0.2276	0.0105	0.0683	0.1015
	3.0	3.858	16.67	0.1949	0.1699	0.1512	0.1477	0.0045	0.0466	0.0461
	4.0	4.997	28.34	0.1454	0.1268	0.1160	0.1142	0.0025	0.0308	0.0276
	5.0	6.297	43.34	0.1160	0.1022	0.0919	0.0919	0.0015	0.0239	0.0174
$\beta = 2.0$	1.0	1.211	1.509	0.6585	0.5674	0.5400	0.5321	0.0485	0.1209	0.4178
	2.0	2.451	3.704	0.2971	0.2541	0.2413	0.2264	0.0115	0.0695	0.1122
	3.0	3.611	7.170	0.1949	0.1699	0.1614	0.1473	0.0045	0.0470	0.0527
	4.0	4.758	11.96	0.1454	0.1268	0.1218	0.1218	0.0025	0.0232	0.0305
	5.0	5.895	17.99	0.1160	0.1022	0.0981	0.0981	0.0015	0.0176	0.0199
Cygnus A										
$\beta = 1.4$	1.6	2.031	4.099	0.3779	0.3256	0.2970	0.2917	0.0175	0.0842	0.1610

Figure 1: The flow behind a spherical bow shock in various atmospheres. The top panel shows the velocity of the flow, the bottom panels the density and the pressure. Solid curves: $\beta = 0$, dashed curves: $\beta = 1$ and dotted curves: $\beta = 2$.

Figure 2: The velocity field of the flow between bow shock and contact discontinuity in the frame of the comoving coordinate system for $\beta = 0$ and $R_b = 1$. The bow shock defines the upper edge, the contact discontinuity the lower edge of the field plotted. The AGN which drives the jet is located in this plot at the point ($z = 0, x = 0$) and the tip of the bow shock is at ($z = 0, x = 1$).

Figure 3: Details of the flow pattern shown in Figure 4.1. Left: the flow close to the hot spot. Right: the flow near the x -axis. Note, that the vectors representing the flow velocity have the same length scale in both plots.

Figure 4: Density profile of the flow between bow shock and contact discontinuity. Top: Uniform atmosphere, $\beta = 0$. Bottom left: $\beta = 1$. Bottom right: $\beta = 2$. For all plots $R_b = 3$. The gray scales are normalised such that the density just ahead of the tip of the bow shock is the same in each panel.

Figure 5: Pressure profile of the flow between bow shock and contact discontinuity. Top: Uniform atmosphere, $\beta = 0$. Bottom left: $\beta = 1$. Bottom right: $\beta = 2$. For all plots $R_b = 3$.

Figure 6: Comparison of the density and pressure distribution for various aspect ratios of the bow shock. Left column: density, right column: pressure. From top to bottom: $R_b = 1, R_b = 2, R_b = 4$ and $R_b = 5$. For all plots $\beta = 1$.

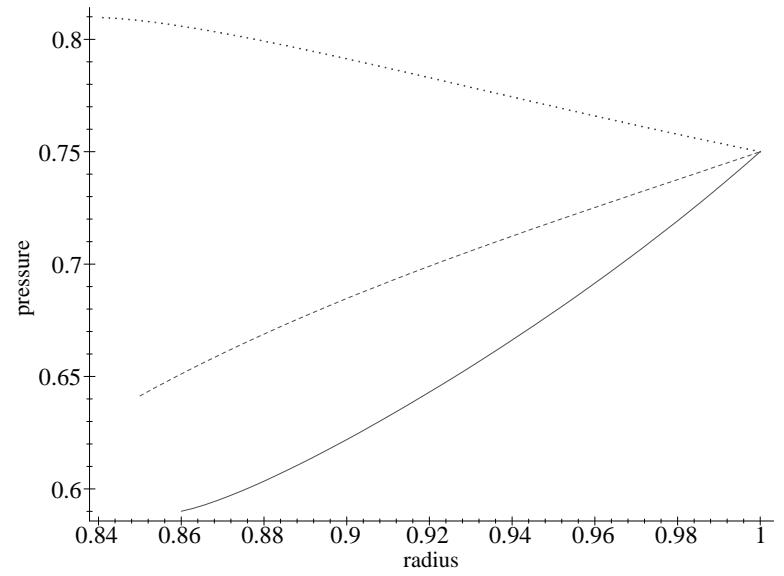
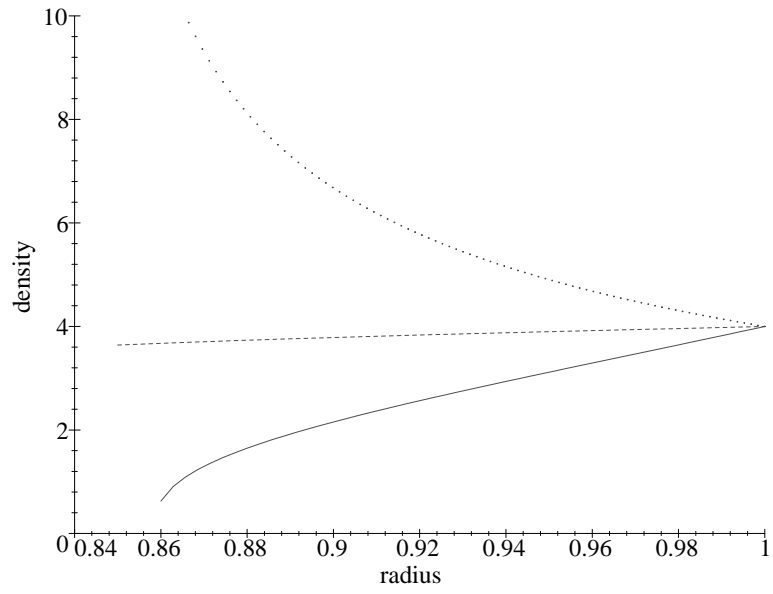
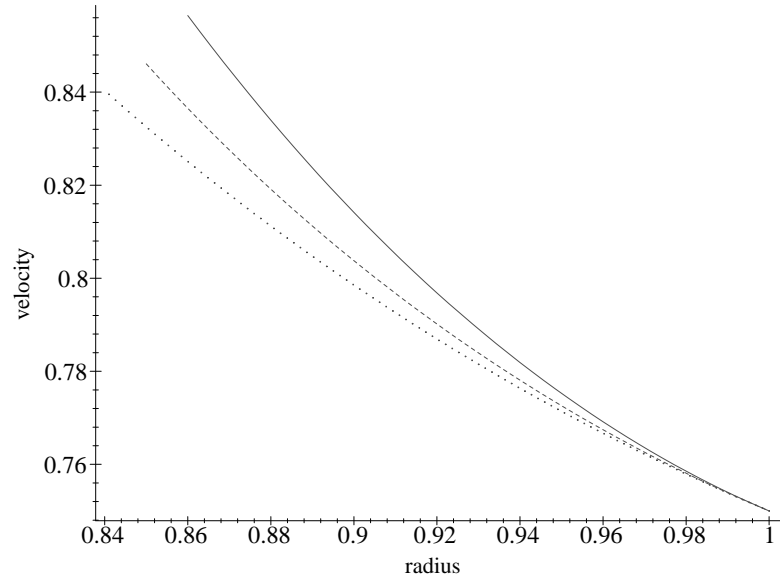
Figure 7: Temperature profile of the flow between bow shock and contact discontinuity. Top: Uniform atmosphere, $\beta = 0$. Bottom left: $\beta = 1$. Bottom right: $\beta = 2$. For all plots $R_b = 3$.

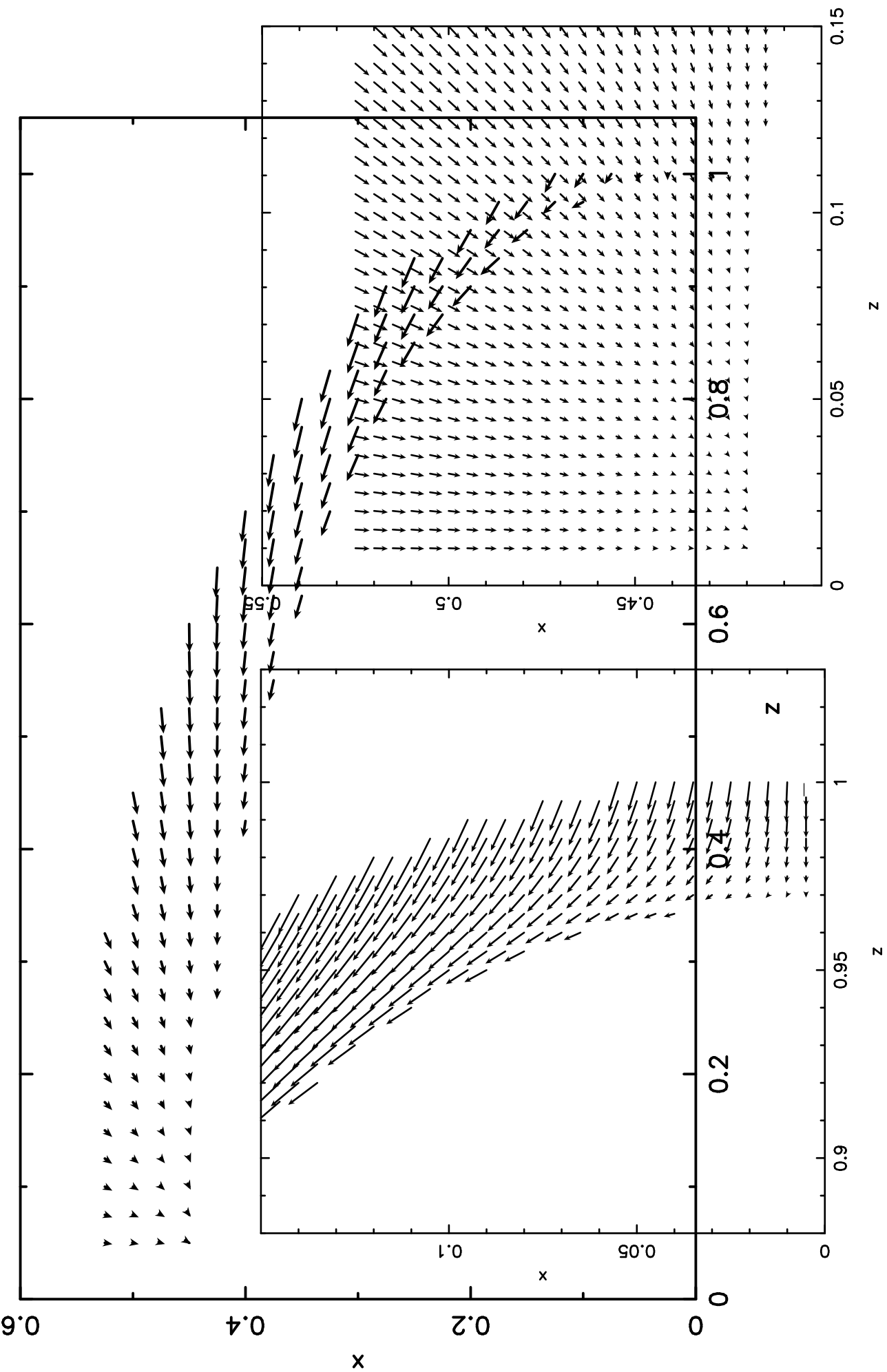
Figure 8: Comparison of the temperature and X-ray surface brightness distribution for various aspect ratios of the bow shock. Left column: temperature, right column: surface brightness. From top to bottom: $R_b = 1, R_b = 2, R_b = 4$ and $R_b = 5$. For all plots $\beta = 1$. For the chosen parameters (see text) the ages of the radio sources in the right column are 3.0×10^7 years, 1.5×10^7 years, 8.8×10^6 years and 7.4×10^6 years respectively from top to bottom.

Figure 9: Surface brightness profile of the flow between bow shock and contact discontinuity. Top: Uniform atmosphere, $\beta = 0$. Bottom left: $\beta = 1$. Bottom right: $\beta = 2$. For all plots $R_b = 3$. See text for the parameters of the external atmosphere and the jet power. The resulting ages of the radio sources are: Top: 3.7×10^7 years, bottom left: 1.1×10^7 years and bottom right: 3.5×10^6 years.

Figure 10: Comparison of the empirical model for the X-ray emission with the numerical calculation. Individual symbols are results from the numerical calculation while curves represent the empirical model. Top panel: $R_b = 1.0$, bottom left: $R_b = 3$ and bottom right: $R_b = 5$. Solid lines and circles: $\beta = 0$, dashed lines and crosses: $\beta = 1$ and dotted lines and squares: $\beta = 2$. See text for other model parameter.

Figure 11: Prolate spheroidal coordinates for $c = 0.6$ and rotation about the z -axis.





This figure "fig4.jpg" is available in "jpg" format from:

<http://arxiv.org/ps/astro-ph/9902018v1>

This figure "fig5.jpg" is available in "jpg" format from:

<http://arxiv.org/ps/astro-ph/9902018v1>

This figure "fig6.jpg" is available in "jpg" format from:

<http://arxiv.org/ps/astro-ph/9902018v1>

This figure "fig7.jpg" is available in "jpg" format from:

<http://arxiv.org/ps/astro-ph/9902018v1>

This figure "fig8.jpg" is available in "jpg" format from:

<http://arxiv.org/ps/astro-ph/9902018v1>

This figure "fig9.jpg" is available in "jpg" format from:

<http://arxiv.org/ps/astro-ph/9902018v1>

